sustainability

MDPI

Article

Analyzing the Stability of Rock Surrounding Deep Cross-Tunnels Using a Dynamic Velocity Field

Yaxun Xiao [1], Shujie Chen [1,2], Zhaofeng Wang [1,*], Liu Liu [1,*] and Canxun Du [3,4]

[1] State Key Laboratory of Geomechanics and Geotechnical Engineering, Institute of Rock and Soil Mechanics, Chinese Academy of Sciences, Wuhan 430071, China; yxxiao@whrsm.ac.cn (Y.X.); chenshujie21@mails.ucas.ac.cn (S.C.)
[2] University of Chinese Academy of Sciences, Beijing 100049, China
[3] Huaneng Tibet Yarlungzangbo River Hydropower Development and Investment Co., Ltd. of No. 12, Beijing West Road, Chengguan District, Lhasa 850008, China; chenpenglin21@mails.ucas.ac.cn
[4] China Huaneng Group R&D Center of Room A312, 3rd Floor, Building 6, Fuxingmennei Street, Xicheng District, Beijing 100031, China
* Correspondence: zfwang@whrsm.ac.cn (Z.W.); liuliu@mail.whrsm.ac.cn (L.L.)

Abstract: With the increasing number of deep rock engineering projects, many different types of tunnels have emerged, such as cross-tunnels. These tunnels intersect with each other in rock, which causes potential safety hazards. We must analyze the stability of the surrounding rock, to ensure worker safety. This article presents a method for dynamically assessing the stability of the surrounding rock in deep-buried cross-tunnels. The method consists of two main analysis steps: (1) P-wave velocity field inversion; and (2) Stability analysis of the surrounding rock. The P-wave velocity field inversion involves inverting the S-wave velocity field by Rayleigh wave and inverting the P-wave velocity field by adjoint state traveltime tomography. Then, a method of stability analysis is proposed which is used to update the mechanical properties of the rock (based on the continuously updated wave velocity field). The elastic modulus of the surrounding rock is approximated throughout the excavation process. CASRock V1.0 (Cellular Automation Software for engineering Rockmass fracturing processes) is used to assess rock damage via the equivalent plastic shear strain and local energy release rate. The new method is used to analyze the stability of a new tunnel excavated in Jinping (in China). The results reveal the severity and spatial distribution of the damage caused. The yield depth is concentrated near the sidewalls, while the top and bottom of the tunnel exhibit a smaller depth. The yield depths present a particular pattern of change (high–low–high–low) with increasing distance from tunnel #2. Finally, this research enriches our understanding of excavating deep cross-tunnels and makes an important contribution to improving worker safety in deep cross-tunnels.

Keywords: deep cross-tunnel; stability analysis; velocity inversion; excavation-damaged zone; CASRock

Citation: Xiao, Y.; Chen, S.; Wang, Z.; Liu, L.; Du, C. Analyzing the Stability of Rock Surrounding Deep Cross-Tunnels Using a Dynamic Velocity Field. *Sustainability* **2023**, *15*, 15139. https://doi.org/10.3390/su152015139

Academic Editor: Jianjun Ma

Received: 13 July 2023
Revised: 3 October 2023
Accepted: 11 October 2023
Published: 23 October 2023

1. Introduction

Rapid economic development has led to an increase in deep rock engineering projects [1]. Deep-buried projects encompass various tunnel types, such as cross-tunnels. Cross-tunnels intersect with each other within rock formations to fulfill specific project requirements [2]. However, excavating new tunnels close to existing tunnels may cause risks to the stability of the surrounding rock. Consequently, this may lead to the formation of significant cracks and other deformations [3]. Hence, it is imperative to conduct an analysis of the stability of the surrounding rock in cross-tunnels, in order to ensure the safety of workers and devices.

The excavation-damaged zone (EDZ) is an important indicator that is used to quantitatively characterize the effects of excavation and stress redistribution in the surrounding rock [4,5]. Excessive rock damage in the EDZ can significantly affect the stability of an engineering structure. Therefore, EDZ is a critical consideration in the analysis of stability [6]. Complex stress interacts when new and old tunnels overlap (including the effects caused by blasting and support operations), which further complicates the development of the EDZ [7].

Using drilling or blasting data to monitor the development of an EDZ has proved to be feasible [8,9]. Specifically, the development of EDZ can be dynamically monitored by inverting the velocity field [10]. The drilling or blasting signals received by sensors can be used to invert the velocity field. However, the times of drilling or blasting events recorded in practice are often imprecise which causes serious challenges when performing traveltime tomography. Accurate timing information is essential for calculating traveltime [11]. Previous studies have shown that the Rayleigh wave is related to the characteristics of an EDZ [12]. Meanwhile, the Rayleigh wave can also be used to invert a layered S-wave velocity field [13]. Therefore, using the Rayleigh wave is a suitable method to obtain the S-wave model of an EDZ. The initial time of a drilling or blasting signal can be calculated by back-propagating rays in the layered S-wave velocity model.

The first-arrival traveltime tomography method is widely recognized as an effective way of inverting velocity fields [14]. Different inversion methods have been developed based on various forward-modeling techniques. For example, tomography has been achieved using ray-tracing techniques based on the shortest path or curved rays, and methods using the eikonal equation and adjoint states [15]. Utilizing the eikonal equation with the fast-marching method (FMM) or fast-sweeping method (FSM) simplifies the complexity of the calculation considerably. Thus, the computation speed can be significantly improved.

The velocity field in a rock is closely linked to its mechanical properties [16]. Continuously updating the velocity field allows for the update of parameters that describe the mechanical properties. These parameters can then be used in numerical simulations to predict the stability of the surrounding rock. Numerical simulations play a crucial role in stability analyses and assessing hazards in rock engineering. Commonly employed techniques include the finite-element method, finite-difference method and discrete-element method, as well as methods using particle flow code, the finite-discrete element method, and the continuum–discontinuum finite-element method [17–21].

Deep rock engineering is characterized by unique geological conditions: high three-dimensional stress, complex spatial relationships, stress paths that change significantly after excavation, and prevalent tension-fracture failure behavior [22]. To address these questions, researchers have developed three-dimensional numerical analysis methods and mechanical models that can effectively capture the geological conditions and deformation characteristics of deep rock masses [23,24]. Appropriate numerical indicators must be used to evaluate the stability of rock masses. Computational analysis-based indicators [25] that are widely used include the yield approach index, failure approach index, brittleness evaluation index, equivalent plastic strain index, energy release rate, and EDZ evaluation. Recently, the degree of rock fracture and local energy release rate (LERR) indicators have been introduced to represent the dominant failure behavior of deep rock masses under tension-fracture failure [26]. These indicators precisely reflect the rupture processes involved, their locations and degrees of severity, and also the energy released locally during the excavation process.

The mechanical parameters chosen to characterize a rock mass have a profound impact on the results of numerical calculations. These values are often determined through methods like laboratory tests, inverse analysis, and direct in situ measurements [27]. However, the direct application of laboratory test results is often inadequate. On the other hand, on site measurements are often costly and very challenging, especially those aimed at determining the rock's cohesive strength or deformation modulus [28]. Recent advancements have enabled the deformation modulus to be estimated via field displacement measurements and inverse analysis [29]. Nevertheless, the accuracy of such measurements is also limited because the accuracy of multi-point displacement meters or tunnel convergence meters is limited. This results in significant time delays and hinders making estimations in real time [27]. Hence, there is an urgent demand for establishing a numerical simulation method that accurately reflects the real-time evolution of mechanical parameters. This is essential for achieving precise stability analyses in deep rock engineering.

In this article, we primarily use a traveltime tomography method to invert the heterogeneous P-wave velocity field based on drilling and blasting data. By converting the inverted P-wave velocity field into material parameters for the rock, the parameter fields can be calculated continuously. These parameter fields are then input into the CASRock (Cellular Automation Software for engineering Rockmass fracturing processes) software to facilitate numerical simulation and analysis. The rock damage (depth, degree, and magnitude) is evaluated using two parameters: the equivalent plastic shear strain (e_{ps}) and LERR. This research aims to lay a foundation for ensuring the safety of workers and services in deep tunnels.

2. Methodology

2.1. Overall Workflow

The workflow involved in our stability analysis method is shown in Figure 1. Two major steps are involved: P-wave velocity field inversion, and stability analysis of the surrounding rock. We outline each of these in turn.

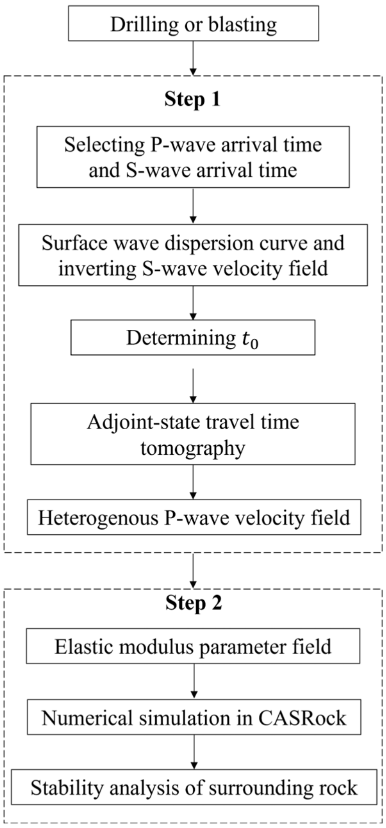

Figure 1. Overall workflow involved in the new stability analysis method.

Step 1: P-wave velocity field inversion

Before inverting the P-wave velocity field, we need to determine an accurate starting timepoint t_0 of the blast concerned. A dispersion curve is extracted from the signals produced by the blast wave using the phase-shift method [29]. The S-wave velocity field can then be obtained via a process of iteration. We need to iterate the velocity field until the dispersion curve of the inverted S-wave velocity field fits that of the real S-wave velocity field. The eikonal equation for the inverted S-wave velocity is then solved by the FMM, in order to yield the traveltimes from the source to the sensors. Then, we can calculate t_0 from the difference between the inverted traveltime and S-wave arrival time.

The adjoint-state traveltime tomography method is then used after every blast to obtain an image of the velocity field. The absolute propagation time of a P-wave can be calculated by the difference between the starting timepoint t_0 and the arrival time of the P-wave. The initial P-wave velocity model for tomography can be estimated by the slope of the P-wave event axis in the wave series and the S-wave layered model. When the difference between the simulated traveltime and absolute traveltime corresponds to the optimal match, the updating process is stopped and the velocity field model is output. The method updates the velocity field in the region between the source and the array of sensors. After each drilling or blasting event, a new velocity field inversion can be performed to obtain a new P-wave velocity field of the surrounding rock.

Step 2: Stability analysis of the surrounding rock

In the case of rock materials, the wave velocity is commonly associated with the Poisson's ratio, elastic modulus, and density of the rock. We assume that the Poisson's ratio and density of the rock remain constant during excavation so that we can perform an approximate calculation. Then the elastic modulus of the rock surrounding the tunnel can be obtained. The elastic modulus parameter field is input into the CASRock V1.0 software to perform numerical simulations. The degree of damage to the surrounding rock is then evaluated by two parameters (e_{ps} and LERR) based on the results from CASRock.

2.2. Adjoint-State Traveltime Tomography

The basic principle of adjoint-state traveltime tomography is to iteratively update the velocity field model until the simulated (theoretical) traveltime data gradually matches the actual traveltime data. The actual traveltime T^{obs} of the signal is calculated via:

$$T^{obs} = t_s - t_0 \tag{1}$$

where t_s is the arrival time of the P-wave recorded by the sensor and t_0 is the time when the blasting event occurred. An objective function J can be defined to evaluate the difference between the observed times and theoretical traveltimes during the inversion process [30]:

$$J(\boldsymbol{c}, t) = \frac{1}{2}\int_{\partial\Omega}\left[t(r) - T^{obs}(r)\right]^2 \mathrm{d}r \tag{2}$$

where $\boldsymbol{c}$ is the velocity field model and r is a sensor in the monitoring section $\partial\Omega$. The time $T^{obs}(r)$ represents the observation time at sensor r, and $t(r)$ represents the theoretical traveltime. $t(r)$ is obtained by solving the eikonal equation for velocity model $\boldsymbol{c}$ by the FMM [31]. To obtain the inverse matrix, an adjoint-state variable (λ) is added to the objective function:

$$J(\boldsymbol{c}, t, \lambda) = \frac{1}{2}\int_{\partial\Omega}\left[t(r) - T^{obs}(r)\right]^2 \mathrm{d}r - \frac{1}{2}\int_{\Omega}\lambda(x)\left[|\nabla t(x)|^2 - \frac{1}{\boldsymbol{c}^2(x)}\right]\mathrm{d}x \tag{3}$$

where $\lambda\ (x)$ is the adjoint-state parameter. To solve the equation, we need to determine the adjoint parameter field λ first:

$$\boldsymbol{m}\cdot\lambda\nabla t = t(r) - T^{obs}(r) \tag{4}$$

$$\nabla\cdot[\lambda\nabla t] = 0 \tag{5}$$

where $\boldsymbol{m}$ is the unit normal vector to the boundary $\partial\Omega$ at position r. Equations (4) and (5) can be solved by the fast sweeping method [32]. Then, we can obtain the gradient formula based on λ:

$$\nabla J(x) = \frac{\partial J}{\partial \boldsymbol{c}} = -\int_{\Omega}\frac{\lambda(x)}{\boldsymbol{c}^3(x)}\mathrm{d}x \tag{6}$$

The gradient of the objective function is defined after introducing the adjoint-state parameters [33]. Finally, we update the velocity field model:

$$\boldsymbol{c}_{n+1} = \boldsymbol{c}_n + \alpha_n \cdot \nabla J_n(\boldsymbol{c}_n) \quad (7)$$

where α_n is the step size used in the nth iteration. When the result for the objective function equation is less than a given threshold, the inversion iteration is stopped to yield the final velocity field model.

The inversion process to find the velocity field in the surrounding rock after each drilling or blasting event can be summarized as follows (Figure 2):

(a) Extract the dispersion curve of the drilling and blasting signals by the phase-shift method [29]. Using the disturbance-inversion method [34], we invert the layered S-wave velocity model. Then, we can obtain the S-wave traveltime by solving the eikonal equation. Combining this with the arrival time of S-wave, the accuracy starting timepoint t_0 of the drilling and blasting event can be calculated.

(b) The observed traveltime $T_k^{obs}(k = 1, 2, \ldots, N)$ is calculated for each sensor according to Equation (1), where N is the numbers of sensors.

(c) The theoretical velocity field model $\boldsymbol{c}_n(i = 1, 2, 3, \ldots)$ is calculated by solving the eikonal equation using the FMM. Adjoint parameters λ are now obtained by solving Equations (4) and (5). Furthermore, λ is substituted into Equation (6) to obtain the gradient $\nabla J_n(x)$ of the objective function.

(d) We use the gradient $\nabla J_n(x)$ and value of α_n to calculate the new speed model $\boldsymbol{c}_{n+1}$. Then, we determine the size of the misfit and the pre-set threshold R. If the misfit is smaller than R, the final speed model $\boldsymbol{c}$ is output; if the misfit is larger than R, we return to step (c).

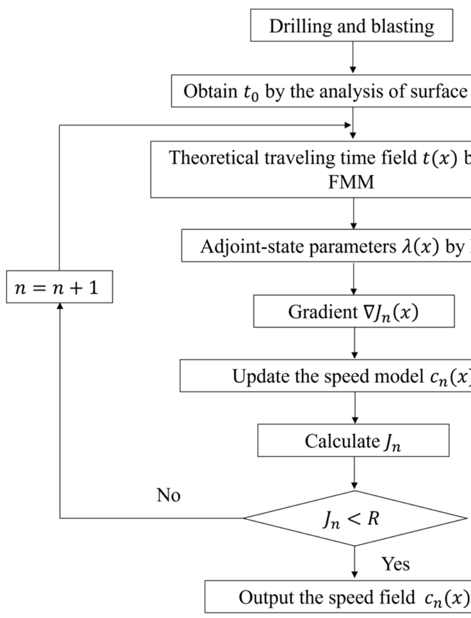

Figure 2. Flowchart for the adjoint-state traveltime tomography method.

2.3. Stability Analysis with Dynamically-Updated Mechanical Properties

2.3.1. Updating the Mechanical Properties

In general, employing the approach outlined in Section 2.2 yields the wave velocity field at a specific location during the excavation process. To enable the mechanical parameters to be updated in real time, it is necessary to convert the wave velocity field into the corresponding mechanical parameter field. In the case of rock materials, the wave velocity is commonly calculated by the following relationship:

$$v = \sqrt{\frac{E(1-\mu)}{\rho(1+\mu)(1-2\mu)}} \tag{8}$$

In the above equation, E, μ, and ρ represent the elastic modulus, Poisson's ratio, and density of the rock material, respectively.

It should be noted that the elastic modulus is strongly affected by historical processes, such as loading and unloading during excavation. This influence is commonly described as 'damage', and can be calculated in accordance with the fundamental definition of damage using the following expression:

$$D = \frac{E_c}{E_0} \tag{9}$$

where E_c represents the current elastic modulus of the rock and E_0 represents its initial elastic modulus. Then, combining this with Equation (8), we obtain the relationship between E_c, E_0 and v_c, v_0:

$$\frac{E_c}{E_0} = \frac{v_c^2}{v_0^2} \tag{10}$$

where v_c represents the current wave velocity, and v_0 represents its initial wave velocity.

However, it should be noted that Equation (8) includes three material parameters related to the rock. To simplify the calculation process, we assume that the rock's Poisson's ratio and density remain relatively constant during excavation and unloading. By adopting this approach, it becomes feasible to calculate the elastic modulus of a specific location promptly.

2.3.2. Simulation Platform

CASRock is a numerical modeling software specifically designed for geotechnical analyses of engineering rock masses [20,22]. Its applications encompass engineering design, predicting safety factors, research and testing, and failure back-analysis. In CASRock, rocks are conceptualized as assemblies of heterogeneous deformable cells that interact with each other. The software enables local mechanical responses (e.g., movement and deformation) to be simulated for each individual cell. It considers the various influences coming from neighboring cells, including external forces, elastoplastic forces, inertial forces, chemical or biological forces, heat, seepage, cracking, invasion, and friction. The state of a cell undergoes a continuum-to-discontinuum transformation, representing the elastic, plastic, and failure stages, which is quantified by an internal variable. Cell interactions follow a self-organizing evolution from the local level to the neighboring cells. The evolution process varies based on the state of the local cell. Global equilibrium is attained following the calculation of each local cell and subsequent propagation of any influences. More detailed information and the principles of CASRock can be found in Reference [35].

CASRock was utilized in this paper to analyze the stability of the surrounding rock. It should be noted that the Mohr–Coulomb strength criterion with tensile cut-off [36] and cohesion weakening and friction strengthening (CWFS) models [37] were adopted for the rock material. In general, this requires just nine parameters: elastic modulus, Poisson's ratio, tensile strength, initial cohesion, initial friction strength, residual cohesion, residual friction strength, ultimate plastic strain associated with cohesion weakening, and plastic strain associated with friction strengthening. In addition, the elastic modulus is updated in real time during the calculation based on the wave velocity field presented in Section 2.2. Meanwhile, the equation of elastic modulus presented in Section 2.3.1 (i.e., Equation (10)). The main parameters needed as input into CASRock are listed in Table 1.

Table 1. Main parameters.

Parameters						
Initial stress conditions	Elastic modulus	Poisson's ratio	Cohesion	Inter friction angle	Tensile strength	Plastic strain

2.3.3. Stability Analysis

In this paper, two indicators are used in the stability analysis: e_{ps} and LERR [25]. The first indicator provides insight into the size of the plastic zone, depth, extent, and magnitude of the damage. This indicator has been extensively used in engineering stability analyses, and has demonstrated its scientific validity and practical applicability [23]. The second indicator (LERR) assesses the amount of energy released during the damage process and provides another indication of the severity of the damage. It has been employed in numerous studies to evaluate the severity of brittle damage phenomena, such as rockbursts [38].

3. Case Study

In this section, we use the new method to analyze the stability of the surrounding rock in the Jinping tunnel. A new tunnel B was excavated by drilling and blasting. We can analyze the stability after each drilling or blasting event with the new method. CASRock is used to analyze the surrounding rock. Some parameters needed as input into CASRock are listed in Table 1. It should be noted that the elastic modulus is updated by the P-wave velocity, while other parameters are approximate estimates from previous studies in Jinping [39–41].

3.1. Background

In 2009, two auxiliary tunnels (tunnels #1 and #2 in Figure 3a) were established between the traffic and drainage tunnels in the Jinping II hydropower station in China (CJPL-II). Recently, a new tunnel B connected to tunnel #2 was designed to be excavated. The relative position and cross-sections of the two tunnels are shown in Figure 3b. The project lies at a depth of 2400 m, where the ground stress at the site was over 60 MPa. Furthermore, the rock surrounding the tunnel is mainly marble, which is brittle and high-strength. Intense rockbursts have occurred frequently in the adjacent diversion tunnels, resulting in several deaths and large-scale destruction of equipment. For example, during the excavation of laboratory D of CJPL-II, an incredibly intense rockburst occurred that nearly destroyed the entire support structure (Figure 3c). The volume of rock violently failing in a brittle manner in the rockburst was about 350 m^3, and the rock burst failure thickness was approximately 3 m. The instability of the rock in the adjacent projects is a serious challenge. It is possible that a complex rock disaster (e.g., rockburst and stress collapse) could occur when the new tunnel B is excavated because of the harsh geological conditions. Thus, the analysis of the surrounding rock is essential for the new tunnel B.

The construction method of tunnel B adopts the drilling or blasting method. The signals produced by the drilling or blasting can be used to invert the wave velocity field. Thus, the stability of surrounding rock can be analyzed by the method proposed in Section 2. To obtain the signals of the drilling or blasting, we can utilize microseismic sensors. The signals produced by rock fracturing or blasting were both recorded in real time.

A sensor array consisting of eight sensors was employed, the layout of which is shown in Figure 4. The arrangement of microseismic sensors follows four principles:

(1) The distance between the drilling and blasting source and sensors must be sufficient to ensure the normal working of sensors.
(2) The location of each sensor is fixed during the excavation of tunnel B.
(3) The sensor array needs to be placed on the same side as the new tunnel B.
(4) The coordinates of different sensors need to be staggered spatially.

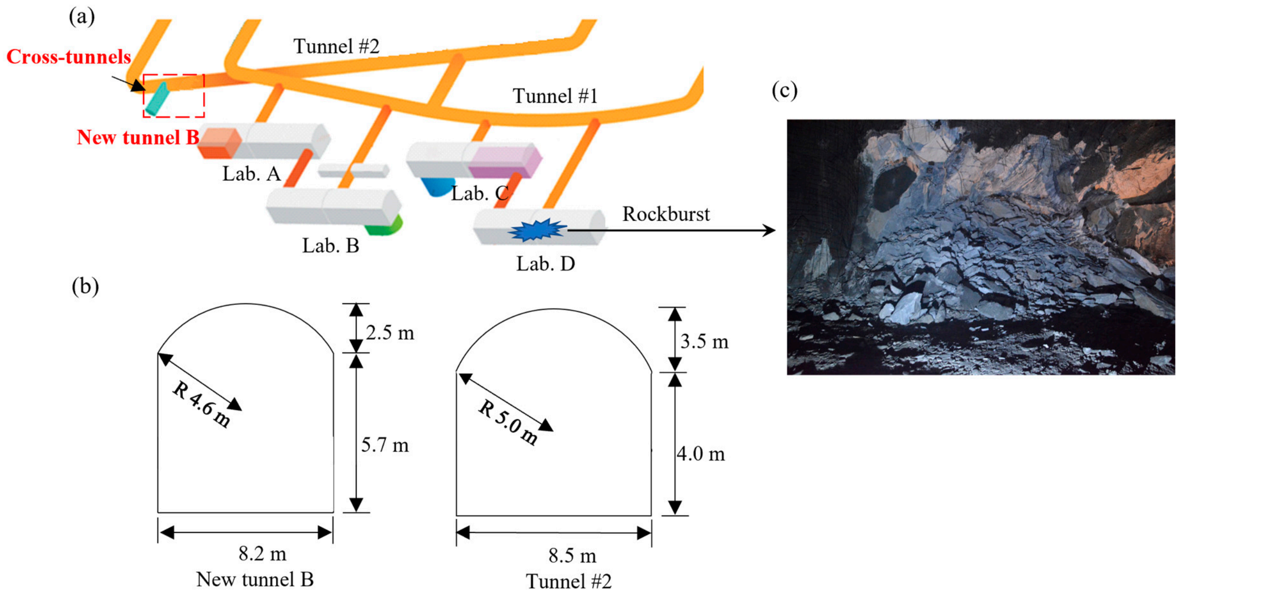

Figure 3. Basic engineering information: (**a**) project layout, (**b**) tunnel cross-sections, and (**c**) photograph of an extremely intense rockburst that occurred in laboratory D of the JinPing project.

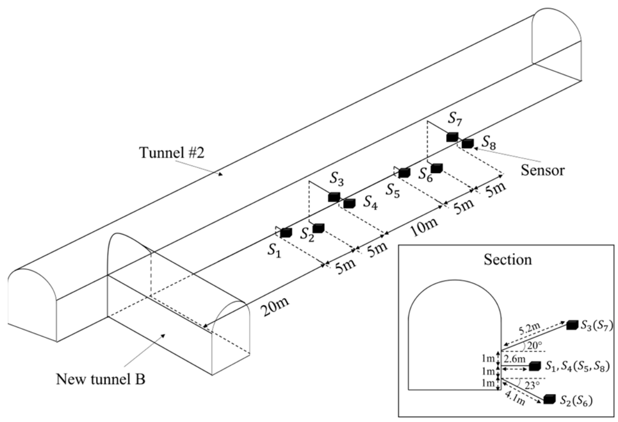

Figure 4. Layout of the microseismic sensors used to monitor rock fracturing in tunnel B.

With the help of microseismic sensors, we can receive blasting signals. The analysis of the stability of the surrounding rock is feasible in this project.

3.2. Tomography Results

The first blast waves recorded by the eight sensors during the excavation of the new tunnel B are shown in Figure 5a. It can be seen that multiple explosions were artificially excited during this blasting event. The waves from each explosion are clearly visible, and there is little interference between the adjacent explosion amplitudes. The first blasting wave is used to invert the P-wave velocity field. Figure 5b shows an expanded view of the wave from the first explosion. It clearly shows the P-waves, which can be identified manually. Four of the sensors (S_1–S_4) are closer to the blasting source than the other four (S_5–S_8). As a result, the arrival time of the S-wave at sensors S_5–S_8 can be more clearly identified. Figure 5c shows that the wave propagates from the source to the sensors S_1, S_4, S_5, and S_8 in turn.

As the distance between the source and sensor increases, the degree of separation between the P- and S-wave gradually increases. In addition, the wave characteristics and arrival times at sensors S_2 and S_3, S_6 and S_7, are found to be very similar. Combining these results with the sensor arrangement shown in Figure 4 (note that S_2/S_6 and S_3/S_7 have different heights compared to the others), it can be expected that the velocity field can be simulated very well in this 2D example.

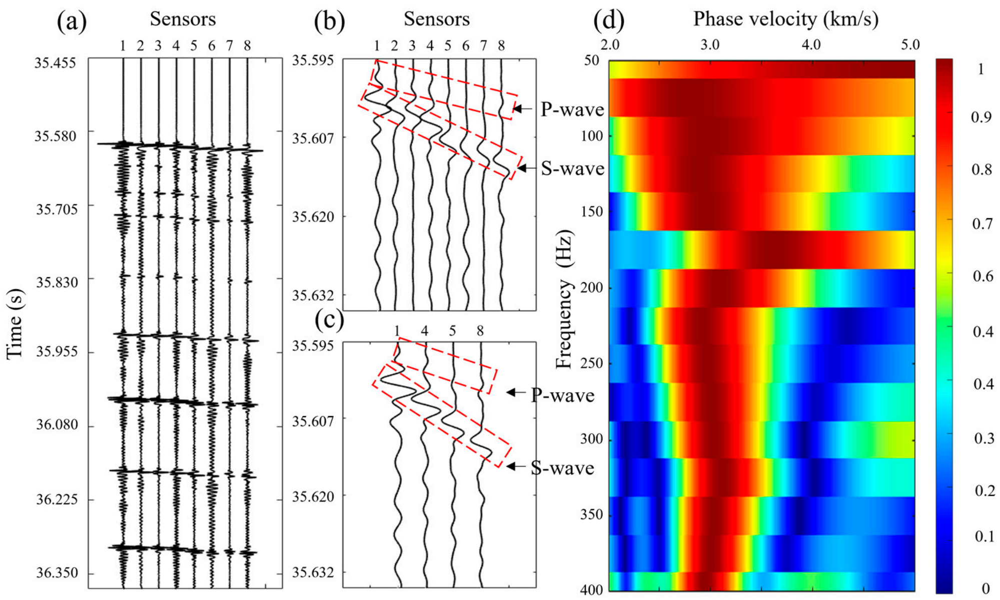

Figure 5. Signal preprocessing: (**a**) the first blast wave from tunnel B; (**b**) time slice of first pulse shown in (**a**); (**c**) time slice for channels S_1, S_4, S_5, and S_8; and (**d**) dispersion curve extracted from the blasting data from tunnel B.

Figure 5d shows the dispersion curve extracted from the blasting signal. The dispersion curve reflects how the phase velocity of a propagating surface wave varies with frequency. The speed at higher frequency tends to be low, while higher speeds are found at frequencies between 50 and 175 Hz. Using the dispersion curve, the layered S-wave velocity model can be inverted using the improved perturbation-inversion method [34].

In the initial layered S-wave velocity model, the velocity increases with depth, as shown in Figure 6b. On the other hand, the final inverted layered S-wave velocity, which is also shown in Figure 6b, exhibits nonlinear changes with depth. Figure 6a shows that the dispersion curve obtained using the inversion results is very close to the actual dispersion curve observed. It can, therefore, be considered that the inverted layered S-wave velocity model is both reasonable and accurate.

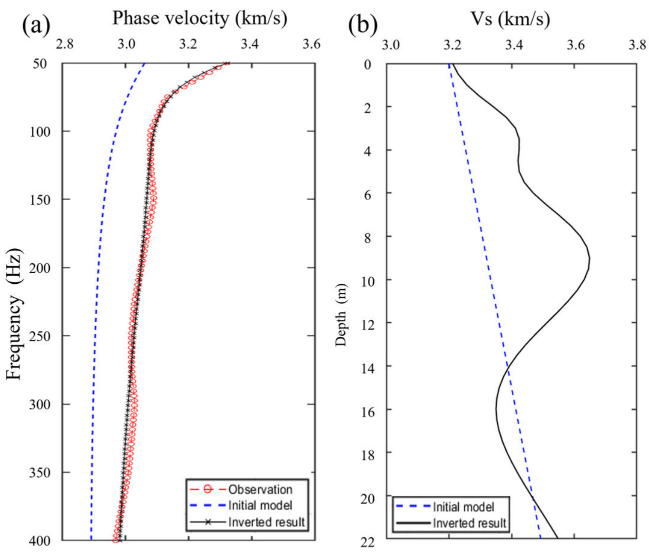

Figure 6. Inversion results produced using the dispersion curve: (**a**) dispersion curve comparison, (**b**) S-wave velocity comparison.

The FMM can now be used to solve the eikonal equation for the inverted layered S-wave velocity model. The results yield the traveltimes of the S-waves propagating from the blast source to the eight sensors. Combining these results with the manually selected S-wave arrival time, t_0 can be calculated to be 23:19:51.64450 on 1 September 2021. The value of t_0 is now used to estimate the absolute traveltimes of the P-waves and P-wave velocity field tomography by the adjoint-state method. The imaging results are shown in Figure 7.

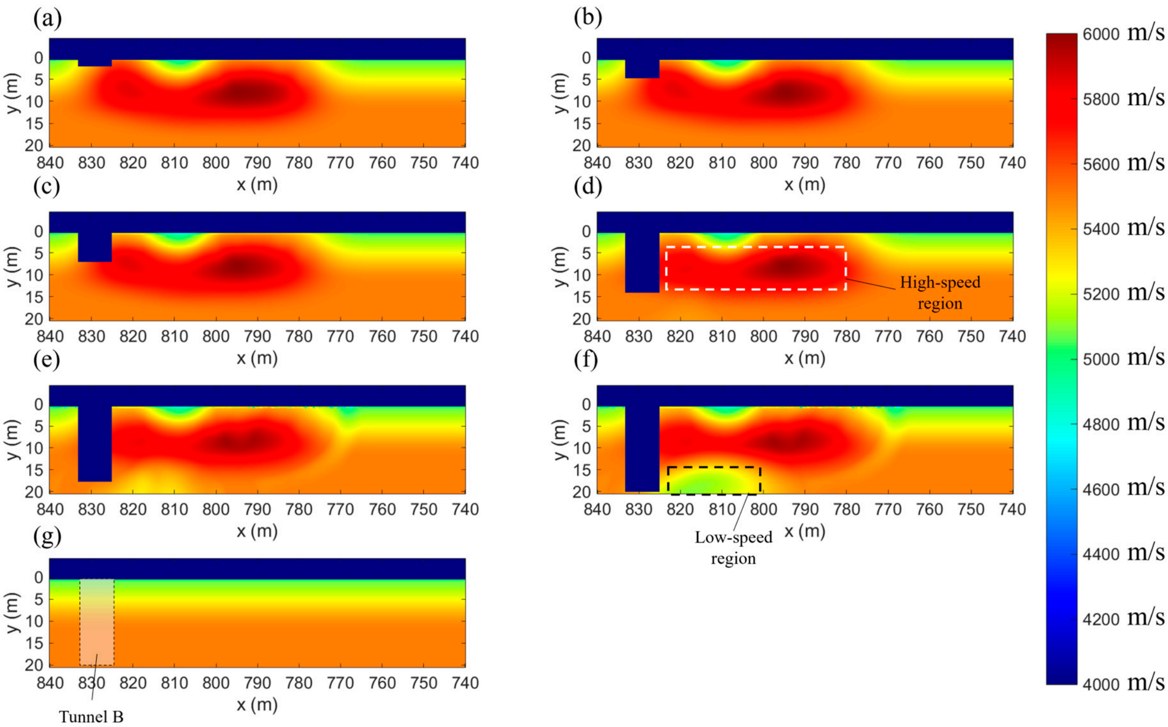

Figure 7. Results of the P-wave traveling time tomography calculations performed during the exaction process. The plots show the tomography results from the (**a**) first, (**b**) second, (**c**) third, (**d**) fourth, (**e**) fifth, and (**f**) sixth blasting sources. (**g**) The initial velocity field model.

The initial velocity field is shown in Figure 7g. The other plots in Figure 7 show how the velocity field between the source and sensor array changed as the excavation process proceeded. The inversion results show that the high-speed region of the velocity field (white dashed box in Figure 7d) is consistent in Figure 7a–d. It also implies that the velocity is relatively high in these parts at depths of 4–10 m. However, the velocity field does not change significantly in the depth range 15–20 m. This is because the ray traces from the sources to the sensors do not travel through this area. However, the velocity field in this area is updated as the rays gradually pass through these deeper rocks (Figure 7e,f) when the depths of the sources increase further.

The black dashed box in Figure 7f highlights a region where the velocity is significantly lower than that in the 4–10 m depth range. The inverted velocity fields can be used to identify the EDZs at different depths. In the present case, the inverted velocity fields suggest that the integrity of the deeper (15–20 m) rock is relatively poor.

3.3. Stability Analysis Results

3.3.1. Simulation Setup

Figure 8 illustrates the fundamental configuration employed in the simulations of this study. As shown in Figure 8a, a relatively large rectangular model is used that measures 100 m × 100 m × 200 m. The longer dimension (200 m) corresponds to the direction of the axis of tunnel #2, which pass through the entire model. Significantly, our main research object is new tunnel B, which is located near the center of the model. The size of the model ensures that the boundaries of the model are 3–5 times the diameters of both auxiliary tunnel #2 and tunnel B (see geometries displayed in Figure 3b).

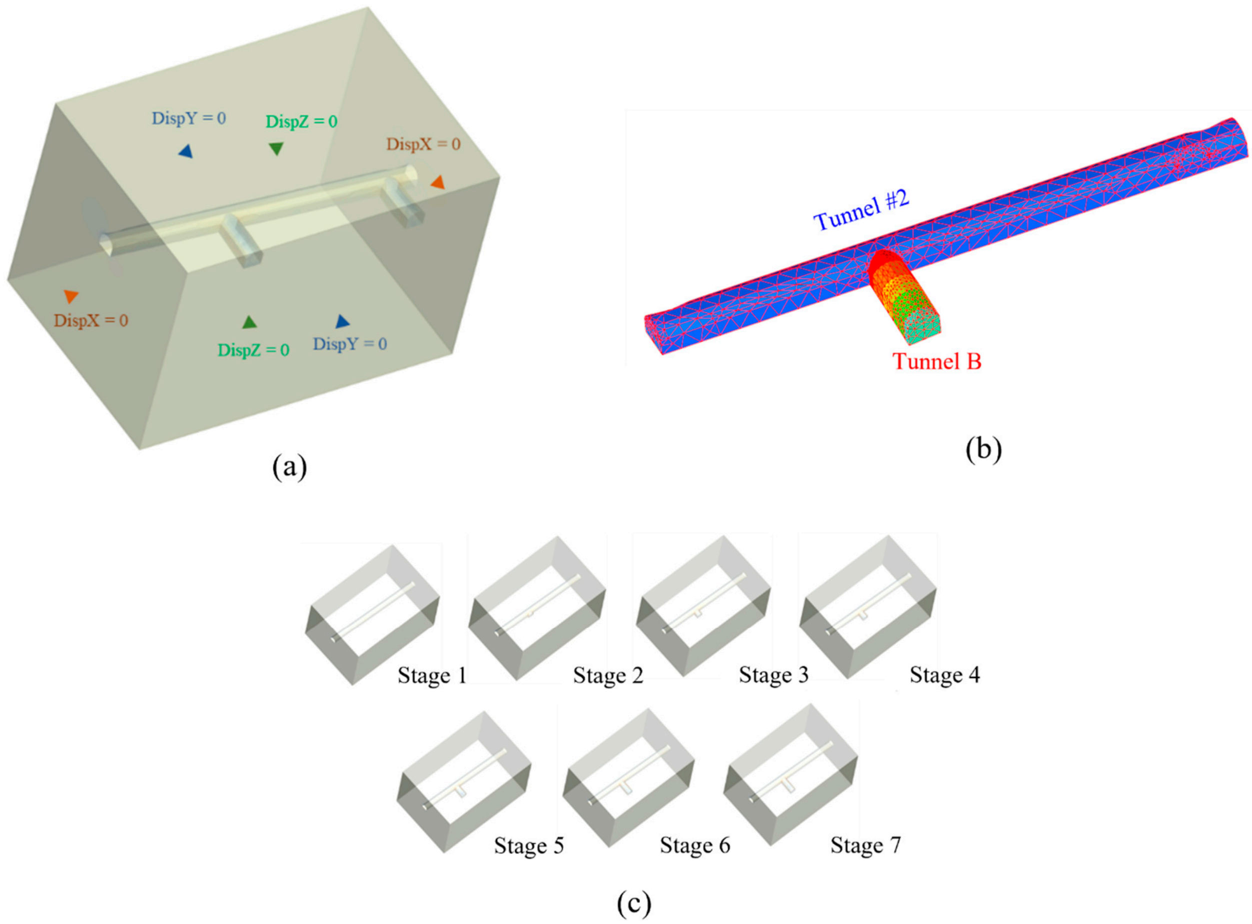

Figure 8. Details of the simulation setup. (**a**) The geometrical model and boundary conditions. (**b**) The grids used to model the tunnels. (**c**) Stages used in the excavation process.

Displacement constraints were applied to all six faces of the rectangular model during the loading process. In detail, the left and right faces were constrained to zero along the X-direction, the front and back faces were constrained to zero along the Y-direction, and the top and bottom faces were constrained to zero along the Z-direction. Figure 8b illustrates the mesh used to model tunnel #2 and tunnel B. Overall, a tetrahedral meshing approach was employed in our simulations. The grid resolution for tunnel #2 was set to 0.5 m, while that for tunnel B was 0.1 m. The remaining areas used a grid resolution of 2 m. Finally, the entire model was divided into 101,706 grids with different sizes. After the completion of the auxiliary tunnel, the excavation of tunnel B proceeded in accordance with the real excavation timeline. Figure 8c presents the specific excavation stages.

The damage criterion and mechanical model presented in Section 2.3.2 were used with the parameter values specified in Tables 2 and 3. The elastic modulus update process starts from stage 2 (Figure 8c). It should be noted that the elastic modulus is updated throughout the excavation process by the algorithm in Section 2.3.1. Figure 9 shows how the elastic modulus varied at different stages of the excavation process. The overall trends are in line with the plots shown in Figure 7. It is essential to clarify that our study is focused solely on investigating the impact of tunnel #2 on the excavation of tunnel B. Thus, this study ignores changes in the wave velocity field and elastic modulus when tunnel #2 was excavated. Additionally, updating the wave velocity field discussed in Section 2.2 starts from stage 2.

Table 2. Initial stress conditions.

σ_x (MPa)	σ_y (MPa)	σ_z (MPa)	τ_{xy} (MPa)	τ_{yz} (MPa)	τ_{zx} (MPa)
47.56	54.55	62.19	4.52	2.35	15.14

Table 3. Main mechanical parameters.

Parameter	Initial	Peak Stress	Residual
Elastic modulus (GPa)	29.2	Updated	Updated
Poisson's ratio	0.23	0.23	0.23
Cohesion (MPa)	35.0	25.9	7.8
Internal friction angle (°)	30.0	37.0	51.0
Tensile strength (MPa)	1.5	1.5	1.5
Plastic strain (‰)	0.0	2.0	6.0

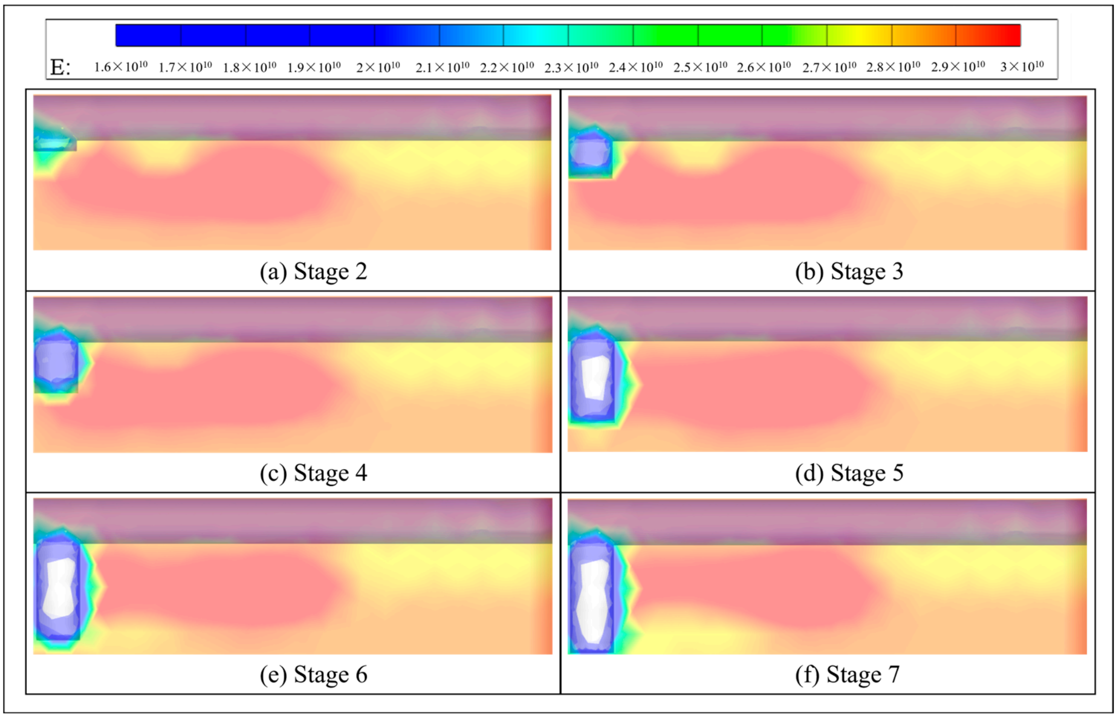

Figure 9. Updating the elastic modulus during the excavation process. The images correspond to stages: (**a**) 2, (**b**) 3, (**c**) 4, (**d**) 5, (**e**) 6, and (**f**) 7 in Figure 8c.

3.3.2. Temporal Failure Characteristics

Figure 10 presents e_{ps} contours calculated along slices in the *YZ*-, *XZ*-, and *XY*-planes during the excavation of tunnel B (i.e., stages 1 to 7). These images highlight the plastic zones in the surrounding rock. As can be seen, the extent of the plastic zone, and hence, the degree of damage progressively increases during the first four excavation stages. However, the contours change minimally after stage 5. This suggests that the majority of the damage develops primarily during the first four excavation stages (ignoring the effects of support systems). Furthermore, the rate of damage growth is most rapid from stage 1 to 2. Less additional damage occurs from stage 2 to 3, even less from stage 3 to 4, and subsequent changes (from stage 5 to 7) are negligible. This implies that as excavation progresses, there is a gradual deceleration in the rate of damage development. Therefore, the most significant damage (in extent and degree) occurs within the first 4.5 m of excavation (i.e., prior to stage 3).

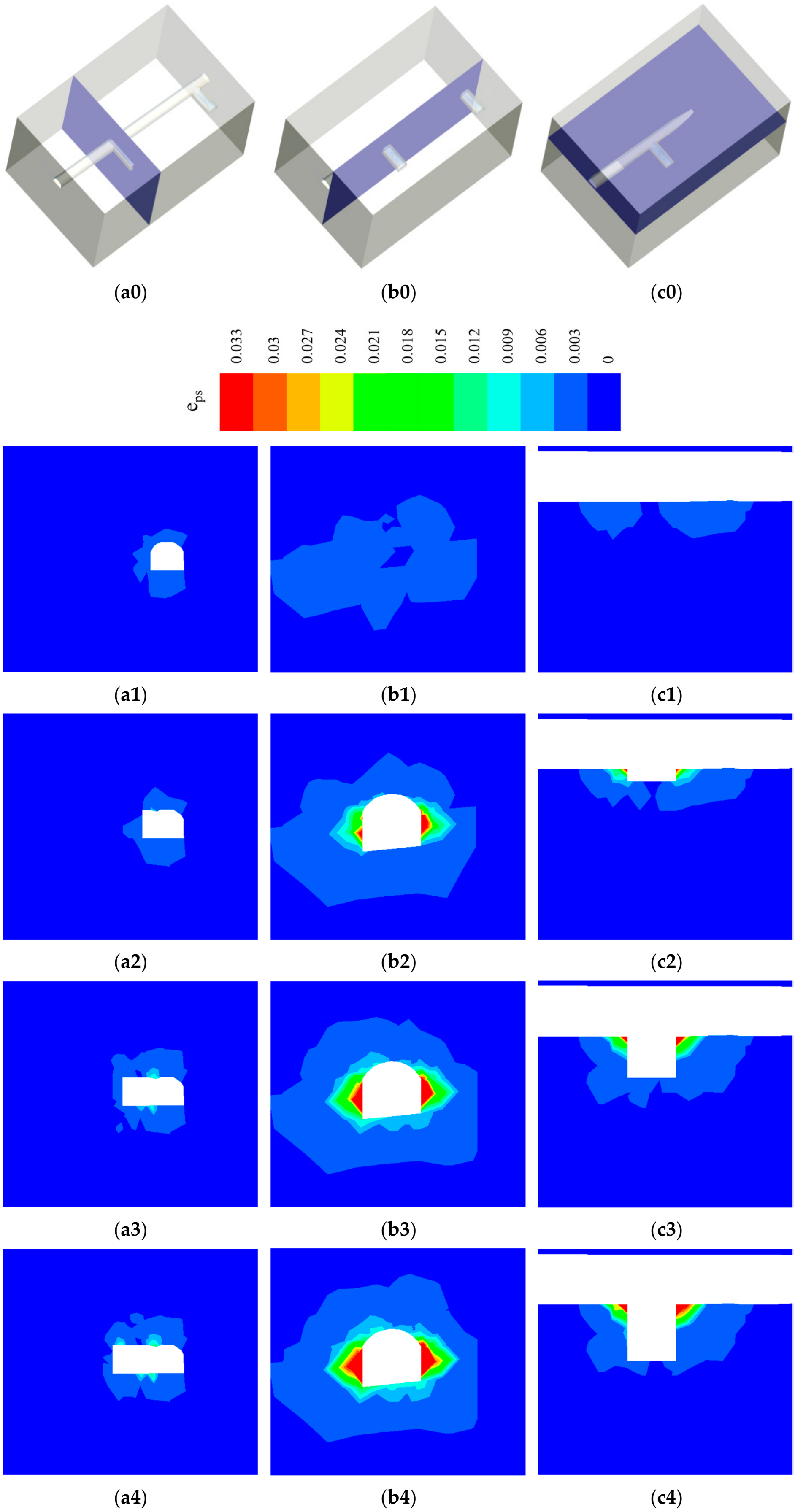

Figure 10. *Cont.*

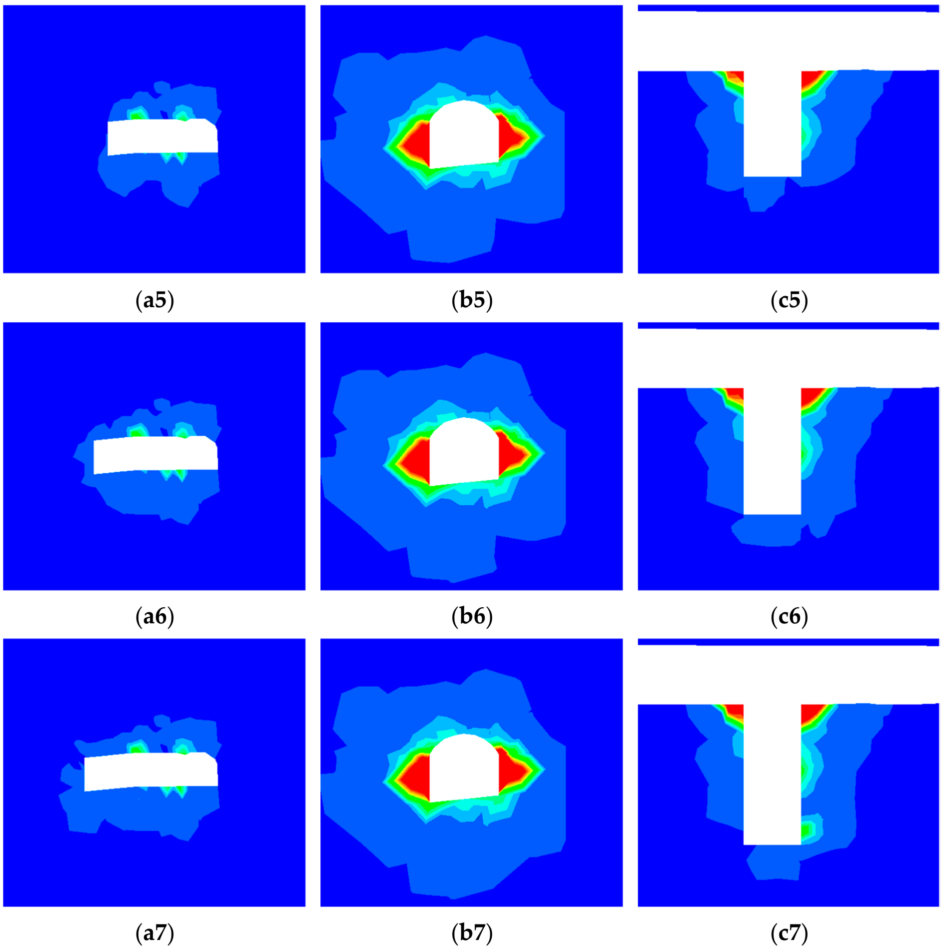

Figure 10. Temporal changes in e_{ps} contours during the excavation of tunnel B. Columns (**a**–**c**) represent slices along the *YZ*-, *XZ*-, and *XY*-planes, respectively, which are shown in the top row. The notation (**a0**,**b0**,**c0**) shows three locations of cross sections that will be observed. The notation (**a***n*), (**b***n*), and (**c***n*) refer to e_{ps} contours corresponding to the *n*th stage, where $1 \leq n \leq 7$.

3.3.3. Spatial Failure Characteristics

Figure 11 presents the Epstn and LERR results for tunnel B at various distances from the auxiliary tunnel just after the completion of excavation stage 7. The Epstn results in the second column of Figure 11 reveal a clear trend–the closer the proximity to tunnel #2, the larger the plastic zone and more severe the damage. Figure 11(b0), corresponding to a distance of 0 m from tunnel #2, clearly exhibits the most extensive amount of damage. Adjacent to the sidewalls, all the Epstn values surpass 0.03. Over the distance from 4 m to 18 m, the maximum Epstn values range from approximately 0.012 to 0.018. When the distance is 16 m, the Epstn value is merely ~0.006.

Similar spatial trends are found in the LERR results. That is, moving away from tunnel #2, the extent and magnitude of the energy release diminishes. It should be noted that the sidewall on the left in Figure 11(b18) and Figure 11(c18) exhibits slightly higher levels of damage and energy release. This is due to the proximity of the wall to the excavated palm face. Nevertheless, this does not impact the overall trend: the damage extent and energy release decreases with increasing distance from tunnel #2.

In this work, the threshold of the e_{ps} value is 0.006 (as shown in Table 3). The rock is considered to be completely destroyed when the e_{ps} value is beyond 0.006. We define the 'yield depth' to be the maximum depth from the sidewall at which the e_{ps} value exceeds 0.006. A quantitative analysis of the results allows a comparison to be made between the yield depth and maximum energy release rate, as shown in Figure 12.

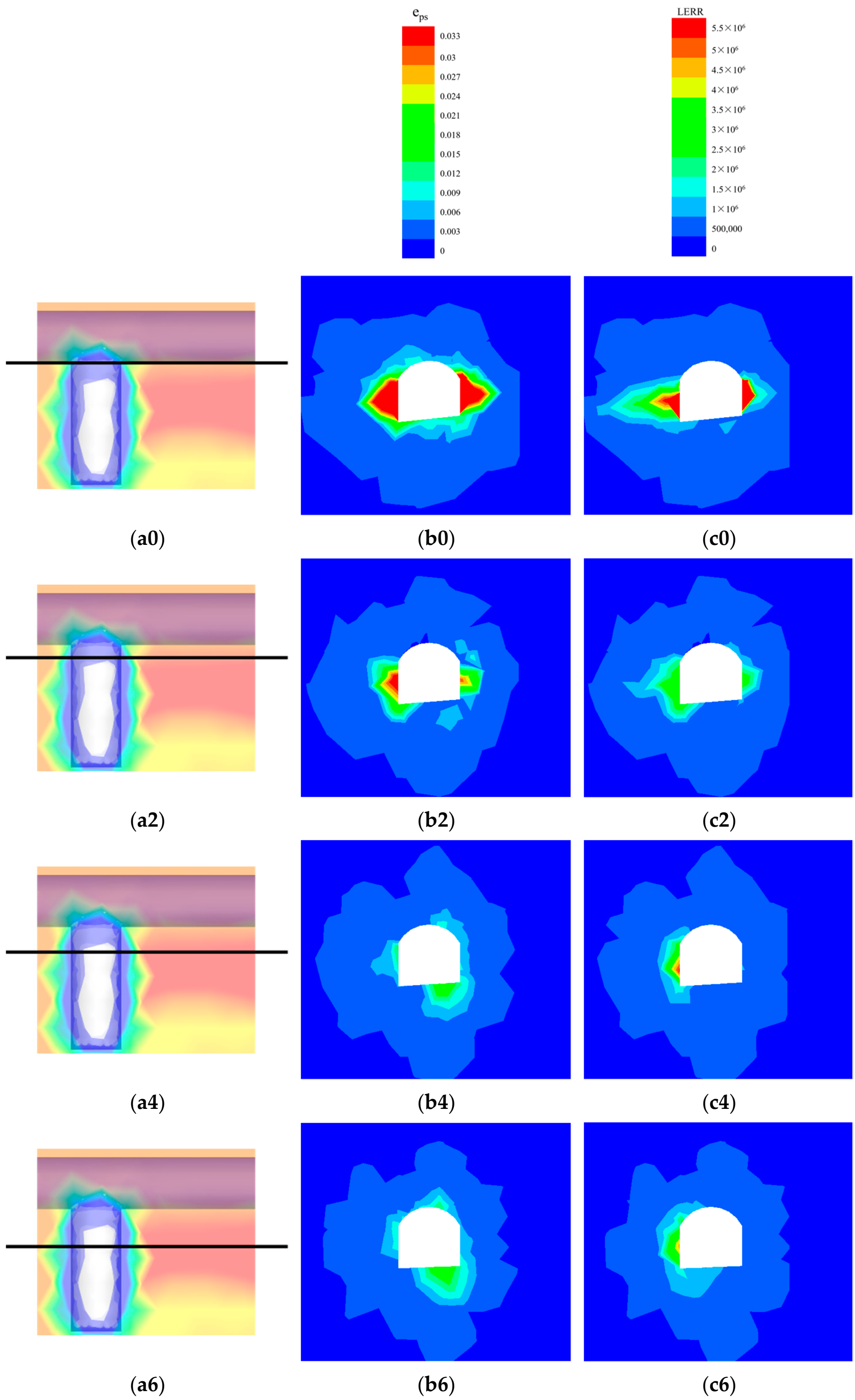

Figure 11. *Cont.*

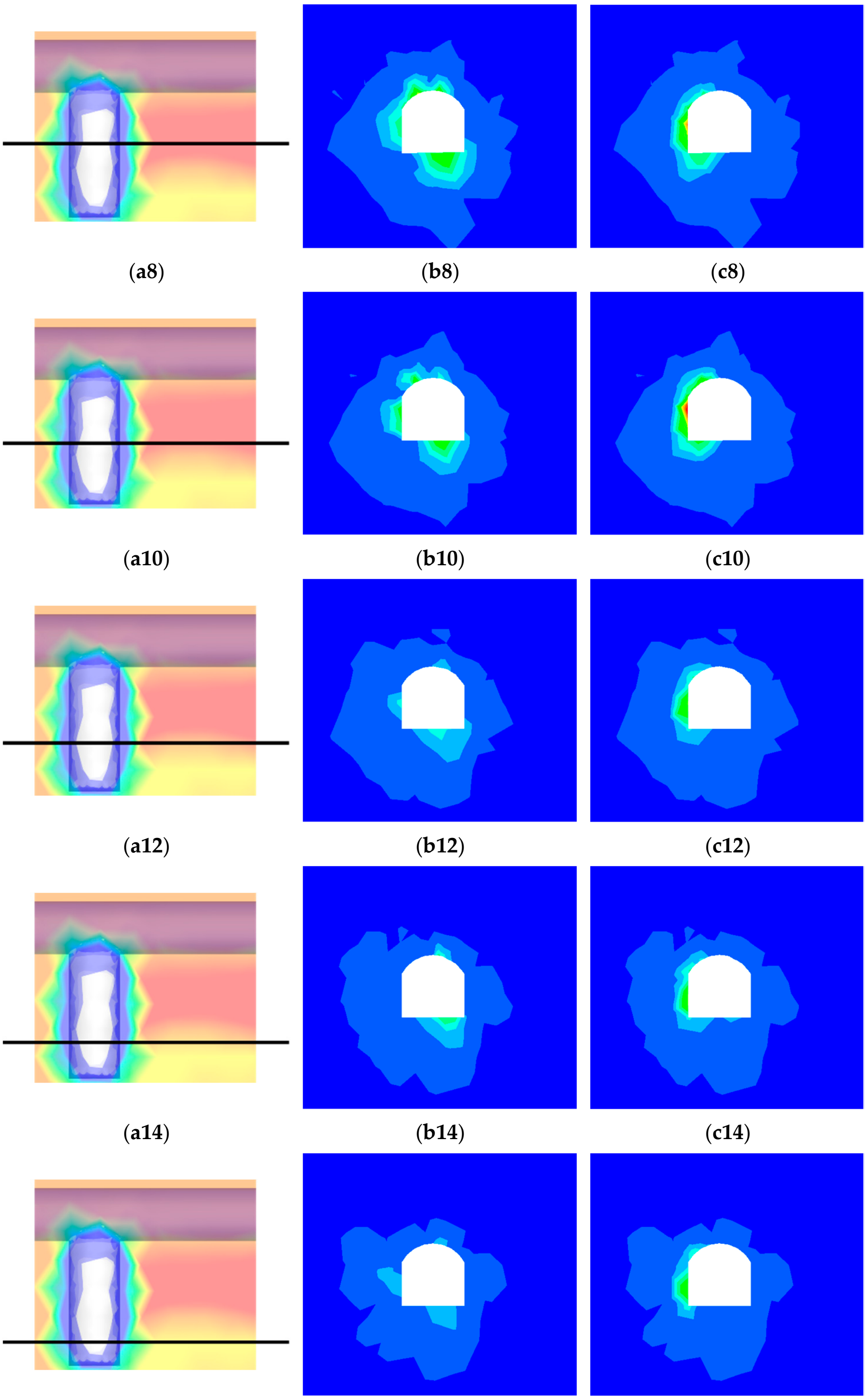

(a8) (b8) (c8)

(a10) (b10) (c10)

(a12) (b12) (c12)

(a14) (b14) (c14)

(a16) (b16) (c16)

Figure 11. *Cont.*

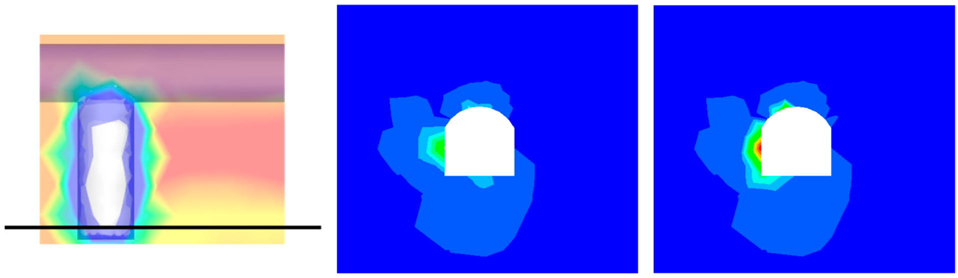

Figure 11. Spatial characteristics of the e_{ps} and LERR results. (**a**) Plan view showing the plane (black line) corresponding to the contours shown. (**b**) e_{ps} contours for the plane. (**c**) LERR contours for the plane. The numbers (0), (2), . . ., (18) represent the distance from tunnel #2 in meters.

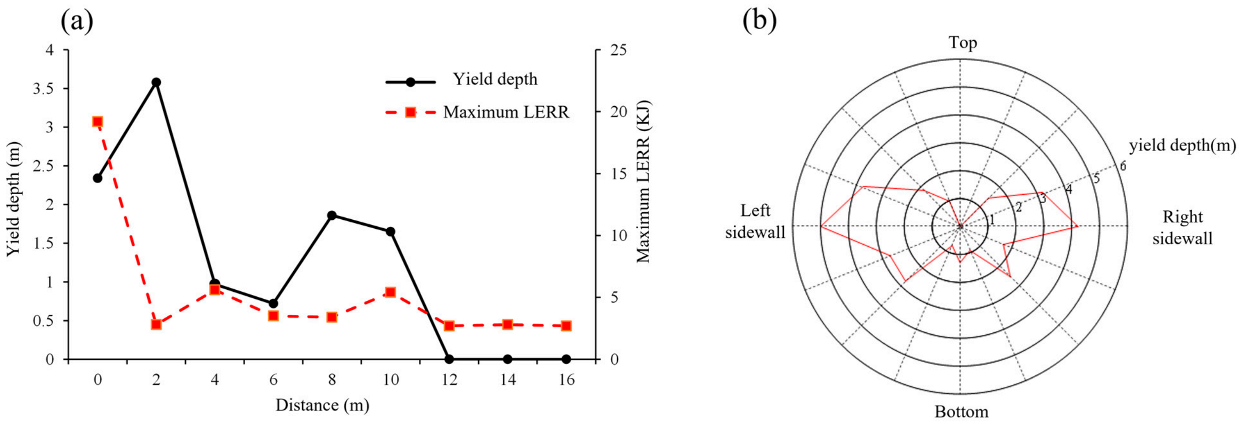

Figure 12. Spatial variation of the yield depth and maximum energy release rate. (**a**) Evolution of yield depth and maximum energy release with distance from tunnel #2. (**b**) Distribution of yield depth across a cross-section of tunnel B.

Figure 12a shows that the yield depth and energy released progressively decrease as the distance from tunnel #2 increases. This is consistent with the contour plots shown in Figure 11. The yield depths for different parts of the tunnel are further illustrated in Figure 12b, which provides a cross-sectional view of their variation. It is evident from this (Nightingale) distribution map that the largest yield depths are concentrated near the left and right sidewalls of the tunnel. Furthermore, the yield depth can be as large as 5 m. In contrast, the yield depths at the top and bottom of the tunnel are much smaller.

Figure 12a suggests that the yield depth peaks in the 0–2 m range, decreases in the range 4–6 m, and then reaches a second peak in the 8–10 m range. There is a high–low–high–low regional variation in the yield depth. Likewise, the maximum energy release is highest at 0 m and exhibits additional local extremes at 4 m and 10 m. These intriguing findings may be because of the presence of a zone with increased wave velocity or elastic modulus in the 4–10 m distance range. In the Section 4, we further explore the effect of updating the elastic modulus in real time on the damage zone and the extent of energy release, delving into these interesting observations.

4. Discussion

We apply the new method to analyze the stability of the surrounding rock in the Jinping tunnel. There are some issues that need to be further studied.

(1) Comparison with traditional stability analysis method

Figure 13 presents a comparison between conventional method and the new method proposed in this article. The contour plots of the e_{ps} values calculated by the continuously updated elastic modulus are shown in Figure 13a,b. Meanwhile, the contour plots of the

e_{ps} values calculated by the conventional method are shown in Figure 13c,d. The results in Figure 13a,c relate to cross-section 'A' in Figure 13b,d (i.e., 2.5 m from the tunnel #2).

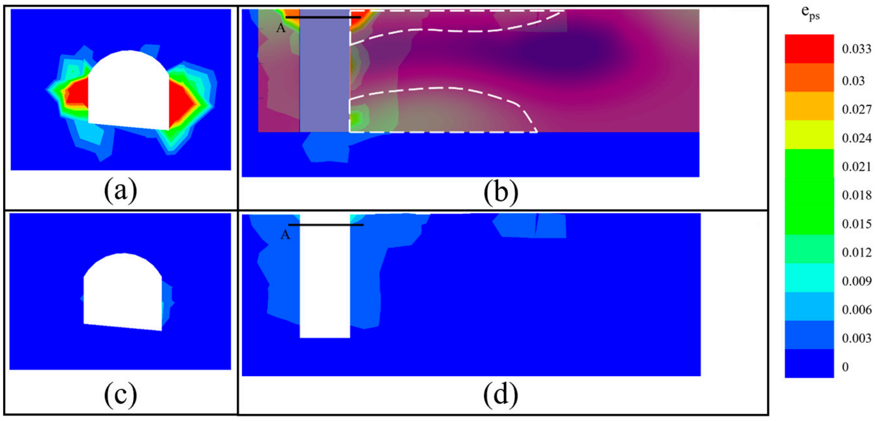

Figure 13. Comparison of e_{ps} contours calculated using the conventional method (**bottom** row) and our new method (**top** row). In (**a**,**b**), the modulus of elasticity is updated in real time and (**a**) is a cross-sectional view taken along the line A in (**b**), which is a plan view. (**c**,**d**) are the equivalent plots simulated using a constant modulus of elasticity.

The simulations predict a much greater level of damage in magnitude and extent when the elastic modulus is updated. In the field, severe damage is found to occur near A. Thus, the traditional method fails to adequately reflect the field damage (Figure 13c,d). However, the new method effectively addresses this limitation of the traditional method by dynamically updating the elastic modulus (Figure 13a,b).

It must be remembered that the excavation of tunnel B commenced sometime after auxiliary tunnel #2 was excavated. Consequently, an EDZ would have formed around tunnel #2 before the excavation of tunnel B. This can be observed in the wave velocity field monitored, as shown in the white dashed box in Figure 13b. The creation of an EDZ will cause stress concentrated in regions further from the tunnel, leading to a more compacted rock mass at a distance of 4–10 m from tunnel #2. This explains the increase of the local wave velocity zone in Figure 13b. In areas where the wave velocity and elastic modulus are both high, the ability of the rock mass to store energy increases. This results in more significant elastoplastic deformation and a corresponding decrease in the degree of energy release. The phenomenon explains the high–low–high–low zonal variation in the yield depth depicted in Figure 12a. Furthermore, this trend of increased elastoplastic deformation at high wave velocities and high elastic modulus is particularly evident. For example, the small region with high e_{ps} values is observed near the tunnel sidewalls between the two dashed boxes in Figure 13b. In contrast, Figure 13d fails to capture the regional nature of the elastoplastic deformation caused by the excavation of tunnel #2. Essentially, the damage is most significant close to auxiliary tunnel #2, with the e_{ps} values falling below 0.003 at all other locations.

(2) Parameters calculation

The analysis of the surrounding rock in CASRock requires many mechanical parameters. This article proposes a method that dynamically updates the elastic modulus calculated by the P-wave velocity field. Other mechanical parameters are estimated by previous studies [38–40]. Because the Jinping project has been conducted for years, many experiments and numerical simulations have fully studied the geological conditions and mechanical parameters in Jinping. Thus, the parameters input into CASRock in Tables 2 and 3 are reliable.

(3) Sustainability development

With the development of the economy, the number of deep underground projects is increasing. The emergence of cross-tunnels is inevitable. This method can analyze the stability of the surrounding rock in cross-tunnels and indicate a dangerous area. Then, the dangerous area is subjected to strengthening support and other preventive measures. Thus, this method can reduce the occurrence of accidents and economic losses. In addition, environmental damage from the project will be minimized as disaster prevention measures are implemented. Finally, we conclude that the method plays a positive role in social sustainability development.

5. Conclusions

In this article, we develop a method aimed at calculating the stability of the surrounding rock in a deep-buried cross-tunnel in real time. The method is applied in the Jinping II hydropower station. The following conclusions can be drawn:

(1) A method is proposed for analyzing the stability of the surrounding rock during excavation. The method consists of inverting the velocity field dynamically by adjoint-state traveltime tomography and stability analysis based on CASRock. The mechanical properties of the surrounding rock are updated in real time by considering the dynamic changes in the wave velocity field in the rock. The method considers the historical changes occurring in the elastic modulus as unloading proceeds during cross-tunnel excavation. In CASRock, the Mohr–Coulomb strength criterion and CWFS model are integrated. The degree of damage to the surrounding rock can be evaluated using two parameters (e_{ps} and LERR).

(2) We applied the method in the Jinping II hydropower station and obtained some interesting information about the zoning phenomenon induced by the excavation process.

   a. There is a progressive increase in the extent and severity of the damage during the initial stages of the excavation. The most substantial damage occurs within the first 4.5 m of excavation. Close proximity to the auxiliary tunnel correlates with larger plastic zones and increased damage.

   b. A spatial analysis of the distribution of the yield depth in the rock further reveals that the largest yield depths are concentrated near the sidewalls. In contrast, the yield depths at the top and bottom of the tunnel vaults are much smaller. The yield depth exhibits a distinct pattern of variation with distance from the auxiliary tunnel ('high–low–high–low'). The peaks occur in the 0–2 and 8–10 m zones. This pattern may arise due to localized increases in wave velocity.

Author Contributions: Conceptualization, writing—original draft and review, Y.X.; formal analysis, writing—original draft and editing, S.C.; methodology, formal analysis, writing—original draft, Z.W.; methodology, writing—original draft and review, L.L.; writing—original draft and review, C.D. All authors have read and agreed to the published version of the manuscript.

Funding: This research was funded by National Natural Science Foundation of China, grant number 42172317, 52209149 and 42207211.

Institutional Review Board Statement: Not applicable.

Informed Consent Statement: Not applicable.

Data Availability Statement: The corresponding authors can provide more details regarding this research through email.

Acknowledgments: We would like to express our sincere gratitude to those who made efforts in reviewing and editing this article.

Conflicts of Interest: The authors declare that they have no known competing financial interests or personal relationships that could have appeared to influence the work reported in this paper.

References

1. Jing, L. A review of techniques, advances and outstanding issues in numerical modelling for rock mechanics and rock engineering. *Int. J. Rock Mech. Min. Sci.* **2003**, *40*, 283–353.
2. Li, X.G.; Yuan, D.J. Response of a double-decked metro tunnel to shield driving of twin closely under-crossing tunnels. *Tunn. Undergr. Space Technol.* **2012**, *28*, 18–30. [CrossRef]
3. Verruijt, A.; Booker, J.R. Surface settlements due to deformation of a tunnel in an elastic half plane. *Geotechnique* **1998**, *48*, 709–713. [CrossRef]
4. Song, Z.; Liu, H.; Kong, X. Development of excavation damaged zones around a rectangular roadway under mining-induced pressure. *Tunn. Undergr. Space Technol.* **2021**, *118*, 104163. [CrossRef]
5. Chen, Y.X.; Yong, W.X.; Li, C.Q.; Zhou, J. Predicting the Thickness of an Excavation Damaged Zone around the Roadway Using the DA-RF Hybrid Model. *CMES-Comput. Model. Eng. Sci.* **2023**, *136*, 2507–2526. [CrossRef]
6. Chen, X.; Wang, J.G. Stability analysis for compressed air energy storage cavern with initial excavation damage zone in an abandoned mining tunnel. *J. Energy Storage* **2022**, *45*, 103725. [CrossRef]
7. Zhu, W.C.; Wei, J.; Zhao, J.; Niu, L.L. 2D numerical simulation on excavation damaged zone induced by dynamic stress redistribution. *Tunn. Undergr. Space Technol.* **2014**, *43*, 315–326. [CrossRef]
8. Liu, L.; Li, S.J.; Xiao, Y.X.; Chen, S.J.; Wang, Z.F.; Feng, G.L.; Wang, Y. An Inverted Heterogeneous Velocity Model for Microseismic Source Location in Deep Buried Tunnels. *Rock Mech. Rock Eng.* **2023**, *56*, 4855–4880. [CrossRef]
9. Ma, J.; Zhao, J.; Lin, Y.; Liang, J.; Chen, J.; Chen, W.; Huang, L. Study on Tamped Spherical Detonation-Induced Dynamic Responses of Rock and PMMA Through Mini-Chemical Explosion Tests and a Four-Dimensional Lattice Spring Model. *Rock Mech. Rock Eng.* **2023**, *56*, 7357–7375. [CrossRef]
10. Ozaki, Y. First-arrival traveltime tomography for monitoring the excavation damaged zone in the Horonobe Underground Research Laboratory. *Rock Mech. Bull.* **2023**, *2*, 100057. [CrossRef]
11. Hu, J.T.; Qian, J.L.; Cao, J.X.; Wang, X.J.; Wang, H.Z.; Leung, S.Y. Ray-illumination compensation for adjoint-state first-arrival traveltime tomography. *Geophysics* **2021**, *86*, U109–U119. [CrossRef]
12. Leparoux, D.; Côte, P.; Gélis, C. EDZ characterization with surface wave analysis: An experimental and numerical study for defining feasibility in the context of the Tournemire platform (France). *Near Surf. Geophys.* **2012**, *10*, 401–411. [CrossRef]
13. Czarny, R.; Malinowski, M.; Chamarczuk, M.; Cwiekata, M.; Olechowski, S.; Lsakow, Z.; Sierodzki, P. Dispersive seismic waves in a coal seam around the roadway in the presence of excavation damaged zone. *Int. J. Rock Mech. Min. Sci.* **2021**, *148*, 104937. [CrossRef]
14. Taillandier, C.; Noble, M.; Chauris, H.; Calandra, H. First-arrival traveltime tomography based on the adjoint-state method. *Geophysics* **2009**, *74*, WCB1–WCB10. [CrossRef]
15. Wang, J.A.; Park, H.D. Comprehensive prediction of rockburst based on analysis of strain energy in rocks. *Tunn. Undergr. Space Technol.* **2001**, *16*, 49–57. [CrossRef]
16. Zhu, Z.; Ranjith, P.G.; Tian, H.; Jiang, G.; Dou, B.; Mei, G. Relationships between P-wave velocity and mechanical properties of granite after exposure to different cyclic heating and water cooling treatments. *Renew. Energy* **2021**, *168*, 375–392. [CrossRef]
17. Müller, W. Numerical simulation of rock bursts. *Min. Sci. Technol.* **1991**, *12*, 27–42. [CrossRef]
18. Deng, X.F.; Zhu, J.B.; Chen, S.G.; Zhao, J. Some fundamental issues and verification of 3DEC in modeling wave propagation in jointed rock masses. *Rock Mech. Rock Eng.* **2012**, *45*, 943–951. [CrossRef]
19. Hadjigeorgiou, J.; Esmaieli, K.; Grenon, M. Stability analysis of vertical excavations in hard rock by integrating a fracture system into a PFC model. *Tunn. Undergr. Space Technol.* **2009**, *24*, 296–308. [CrossRef]
20. Feng, X.T.; Pan, P.Z.; Zhou, H. Simulation of the rock microfracturing process under uniaxial compression using an elasto-plastic cellular automaton. *Int. J. Rock Mech. Min. Sci.* **2006**, *43*, 1091–1108. [CrossRef]
21. Lin, Y.; Ma, J.; Lai, Z.; Huang, L.; Lei, M. A FDEM approach to study mechanical and fracturing responses of geo-materials with high inclusion contents using a novel reconstruction strategy. *Eng. Fract. Mech.* **2023**, *282*, 109171. [CrossRef]
22. Pan, P.Z.; Feng, X.T.; Hudson, J.A. Numerical simulations of Class I and Class II uniaxial compression curves using an elasto-plastic cellular automaton and a linear combination of stress and strain as the control method. *Int. J. Rock Mech. Min. Sci.* **2006**, *43*, 1109–1117. [CrossRef]
23. Hajiabdolmajid, V.; Kaiser, P.K.; Martin, C.D. Modelling brittle failure of rock. *Int. J. Rock Mech. Min. Sci.* **2002**, *39*, 731–741. [CrossRef]
24. Ma, J.; Chen, J.; Chen, W.; Huang, L. A coupled thermal-elastic-plastic-damage model for concrete subjected to dynamic loading. *Int. J. Plast.* **2022**, *153*, 103279. [CrossRef]
25. Feng, X.T.; Wang, Z.F.; Zhou, Y.Y.; Yang, C.X.; Pan, P.Z.; Kong, R. Modelling three-dimensional stress-dependent failure of hard rocks. *Acta Geotech.* **2021**, *16*, 1647–1677. [CrossRef]
26. Sakurai, S. *Back Analysis in Rock Engineering*; CRC Press: Boca Raton, FL, USA, 2017.
27. Guo, H.S.; Feng, X.T.; Li, S.J.; Yang, C.X.; Yao, Z.B. Evaluation of the integrity of deep rock masses using results of digital borehole televiewers. *Rock Mech. Rock Eng.* **2017**, *50*, 1371–1382. [CrossRef]
28. Feng, X.T.; Xu, H.; Qiu, S.L.; Li, S.J.; Yang, C.X.; Guo, H.S.; Cheng, Y.; Yao, H.G. In situ observation of rock spalling in the deep tunnels of the China Jinping Underground Laboratory (2400 m depth). *Rock Mech. Rock Eng.* **2018**, *51*, 1193–1213. [CrossRef]

29. Park, C.B.; Miller, R.D.; Xia, J. Imaging dispersion curves of surface waves on multi-channel record. In *SEG Technical Program Expanded Abstracts 1998*; Society of Exploration Geophysicists: Tulsa, OK, USA, 1998; pp. 1377–1380.
30. Hole, J.A. Nonlinear high-resolution three-dimensional seismic travel time tomography. *J. Geophys. Res. Solid Earth* **1992**, *97*, 6553–6562. [CrossRef]
31. Kroon, D.J. *Accurate Fast Marching*; MATLAB 2011a; Central File Exchange: Enschede, The Netherlands, 2021.
32. Raydan, M. The Barzilai and Borwein gradient method for the large scale unconstrained minimization problem. *SIAM J. Optim.* **1997**, *7*, 26–33. [CrossRef]
33. Noble, M.; Thierry, P.; Taillandier, C.; Calandra, H. High-performance 3D first-arrival traveltime tomography. *Lead. Edge* **2010**, *29*, 86–93. [CrossRef]
34. Liu, L.; Wang, Y. Perturbational inversion of fundamental mode Rayleigh wave dispersion curve. In Proceedings of the SEG International Exposition and Annual Meeting, Denver, CO, USA, 26 September–1 October 2021; p. D011S075R007.
35. Feng, X.T.; Pan, P.Z.; Wang, Z.F.; Zhang, Y.L. Development of cellular automata software for engineering rockmass fracturing processes. In *Challenges and Innovations in Geomechanics. IACMAG 2021*; Springer International Publishing: Cham, Switzerland, 2021; Volume 125, pp. 62–74. [CrossRef]
36. He, Y.; Liu, Y.; Hazarika, H.; Yuan, R. Stability analysis of seismic slopes with tensile strength cut-off. *Comput. Geotech.* **2019**, *112*, 245–256. [CrossRef]
37. Walton, G. Initial guidelines for the selection of input parameters for cohesion-weakening-friction-strengthening (CWFS) analysis of excavations in brittle rock. *Tunn. Undergr. Space Technol.* **2019**, *84*, 189–200. [CrossRef]
38. Jiang, Q.; Feng, X.T.; Xiang, T.B.; Su, G.S. Rockburst characteristics and numerical simulation based on a new energy index: A case study of a tunnel at 2500 m depth. *Bull. Eng. Geol. Environ.* **2010**, *69*, 381–388. [CrossRef]
39. Feng, X.T.; Xu, H.; Yang, C.X.; Zhang, X.W.; Gao, Y.H. Influence of loading and unloading stress paths on the deformation and failure features of Jinping marble under true triaxial compression. *Rock Mech. Rock Eng.* **2020**, *53*, 3287–3301. [CrossRef]
40. Jiang, Q.; Zhong, S.; Cui, J.; Feng, X.T.; Song, L.B. Statistical characterization of the mechanical parameters of intact rock under triaxial compression: An experimental proof of the Jinping marble. *Rock Mech. Rock Eng.* **2016**, *49*, 4631–4646. [CrossRef]
41. Cui, Z.; Sheng, Q.; Leng, X.L.; Ma, Y. Investigation of the long-term strength of Jinping marble rocks with experimental and numerical approaches. *Bull. Eng. Geol. Environ.* **2019**, *78*, 877–882. [CrossRef]